Fast electron thermometry towards ultra-sensitive calorimetric detection

S. Gasparinetti,[1,*] K. L. Viisanen,[1,†] O.-P. Saira,[1] T. Faivre,[1] M. Arzeo,[2] M. Meschke,[1] and J. P. Pekola[1]

[1] *Low Temperature Laboratory (OVLL), Aalto University, P.O. Box 15100, FI-00076 Aalto, Finland*
[2] *Quantum Device Physics Laboratory, Department of Microtechnology and Nanoscience, Chalmers University of Technology, SE-41296 Göteborg, Sweden*

(Dated: November 6, 2014)

We demonstrate radiofrequency thermometry on a micrometer-sized metallic island below 100 mK. Our device is based on a normal metal-insulator-superconductor tunnel junction coupled to a resonator with transmission readout. In the first generation of the device, we achieve $90\,\mu\mathrm{K}/\sqrt{\mathrm{Hz}}$ noise-equivalent temperature with 10 MHz bandwidth. We measure the thermal relaxation time of the electron gas in the island, which we find to be of the order of 100 µs. Such a calorimetric detector, upon optimization, can be seamlessly integrated into superconducting circuits, with immediate applications in quantum-thermodynamics experiments down to single quanta of energy.

arXiv:1405.7568v2 [cond-mat.mes-hall] 4 Nov 2014

INTRODUCTION

Thermometry is a key in studies of thermodynamics. When investigating large systems, it is often sufficient to monitor time-averaged temperatures, as the relative fluctuations are small. Then the bandwidth of the thermometer may not be an important figure of merit as such. In small systems, on the contrary, temporal statistical variations become increasingly important and it would be of great benefit to determine the effective temperature over time scales shorter than the relevant thermal relaxation time of the measured system. Despite the apparent lack of fast thermometers in mesoscopic structures, interesting experiments in thermal physics have been performed and are under way, including measurements of the quantum of heat conductance [1–3], of Landauer's principle of minimum energy cost of erasure of a logic bit [4], and of information-to-energy conversion in Maxwell's demons [5, 6]. Fast thermometry and calorimetry would tremendously expand the variety of phenomena to be explored, providing direct access to the temporal evolution of effective temperatures under non-equilibrium conditions, the energy-relaxation rates, and the fundamental fluctuations of the effective temperature in small systems. The observation of single quanta of microwave photons would eventually provide a way to investigate heat transport and its statistics in depth [7–9], for example in superconducting quantum circuits.

Here we demonstrate a significant step towards single-microwave-photon calorimetry beyond the seminal experiments in Refs. [10–13], down to electronic temperatures below 100 mK. Our rf-transmission readout of a normal-insulator-superconductor (NIS) tunnel junction provides $90\,\mu\mathrm{K}/\sqrt{\mathrm{Hz}}$ thermometry with a bandwidth of 10 MHz. Based on real-time characterization of the thermal response of the island, we conclude that the measured 100 µs relaxation time would allow us to detect a 10 mK temperature spike in single-shot. Our single-shot resolution has to be enhanced by one order of magnitude in order to finally detect a single 1 K (20 GHz) photon impinging on an optimized absorber.

CHARACTERIZATION

Our technique relies on the temperature-dependent conductance of the NIS junction [14–16]. In the standard dc configuration, the high impedance of the junction, together with stray capacitance from the measurement cables, limits its bandwidth to the kHz range. In order to enable a fast readout, we embed the NIS junction in an LC resonant circuit [11]. Similar techniques are routinely used for the fast readout of high-impedance nanodevices, including single-electron transistors [17] and quantum point contacts [18, 19].

Our sample consists of a 25 nm thick, 100 nm wide and 20 µm long Cu island connected to Al leads via two clean normal metal-superconductor (NS) contacts and a NIS junction with normal-state resistance $R_T = 22\,\mathrm{k}\Omega$. A schematic of our measurement set-up is shown in Fig. 1(a) and a close-up, false-color micrograph of the device is shown in Fig. 1(b). The device is fabricated on top of an oxidized silicon substrate by standard electron-beam lithography, three-angle metal evaporation with in-situ Al oxidation, and liftoff. The NIS probe is embedded in an LC resonator formed by a $L = 80\,\mathrm{nH}$ surface-mount inductor, which together with the stray capacitance $C = 0.5\,\mathrm{pF}$ and coupling capacitors $C_{\mathrm{C1}} = 0.1$ pF, $C_{\mathrm{C2}} = 0.2$ pF gives a resonant frequency $f_0 = 625\,\mathrm{MHz}$. A bias tee allows a dc voltage bias V_b to be applied to the NIS junction without interfering with the resonator readout. Of the two NS contacts, one is grounded at the sample stage, while the other is used to feed a heating current to the island. The total resistance between the normal electrode of the NIS junction and the ground, including the resistance of the NS contact, was measured to be $360\,\Omega$.

We probe the resonator, coupled to input and output ports via the capacitors C_{C1} and C_{C2}, by measuring the transmittance $|S_{21}|^2 = P_{\mathrm{det}}/P_{\mathrm{gen}}$, see Fig. 1(a). For the time-resolved measurements described in the following,

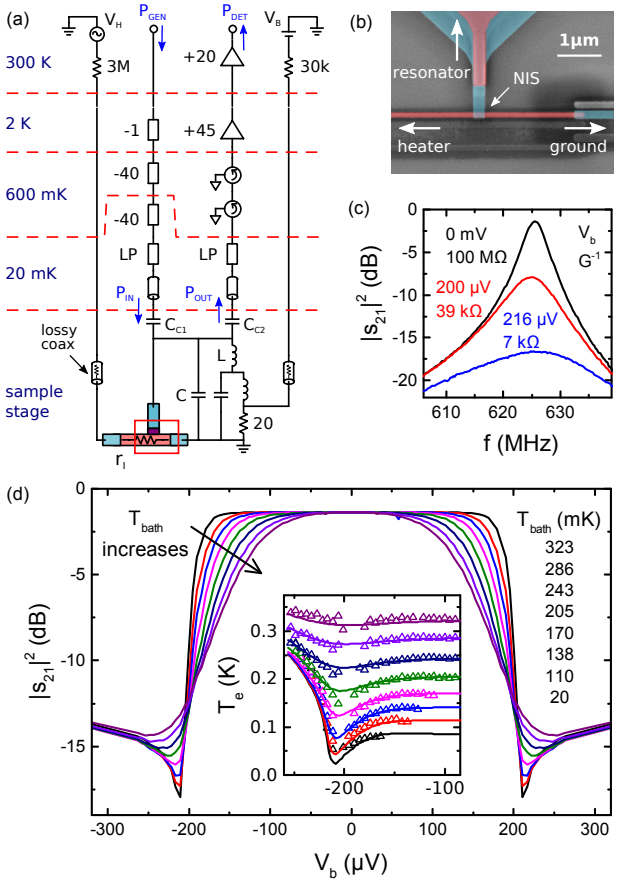

FIG. 1. **The rf-NIS thermometer.** (a) Schematic of the measurement circuit. (b) False-color micrograph of a representative device (red: Cu, blue: Al), closing up on the NIS junction used as a thermometer. (c) Small-signal transmittance $|s_{21}|^2$ versus frequency for three selected values of the voltage bias V_b; the corresponding differential resistance G^{-1} of the NIS junction varies between 7 kΩ and 100 MΩ. (d) Transmittance-voltage characteristics: $|s_{21}|^2$ versus V_b for a set of bath temperatures $T_{\rm bath}$ in the range of 20 to 323 mK. For each temperature, the transmittance at zero bias is taken as the 0 dB reference. Inset: Electronic temperature T_e vs V_b for different values of $T_{\rm bath}$. The experimental points (triangles) are obtained from the data of the main panel using Eqs. (1) and (2). The predictions of a thermal model taking into account electron-phonon and tunneling heat conductance [21] are shown for comparison (solid lines).

the signal is demodulated at the carrier frequency and recorded with a fast digitizer. The rf input line is attenuated by 80 dB below 2 K before reaching the sample stage. Two circulators in series ensure at least 45 dB isolation between the resonator output and a low-noise high-electron-mobility-transistor (HEMT) amplifier mounted on the 2 K plate. The bias and heating lines are filtered by a 2 m long lossy coaxial line (Thermocoax). Sample and resonator are enclosed in an rf-tight, indium-sealed [20] copper box mounted at the base plate of a dilution refrigerator cooled down to 20 mK. The base plate temperature $T_{\rm bath}$ is measured by a calibrated RuOx thermometer.

At low input power, the resonator probes the differential conductance $G = \partial I/\partial V_b$ of the junction at the bias point V_b. Figure 1(c) shows how the resonance peak responds to changes in V_b. The transmittance of the resonator at resonance is given by

$$|s_{21}| = 2\kappa \frac{G_0}{G + G_0} \ , \qquad (1)$$

with $\kappa = C_{C1}C_{C2}/(C_{C1}^2 + C_{C2}^2)$ and $G_0 = 4\pi^2(C_{C1}^2 + C_{C2}^2)Z_0 f_0^2$ (here $Z_0 = 50\,\Omega$ is the transmission line impedance and f_0 is the resonance frequency). By measuring $|s_{21}|^2$ at $V_b = 0$ and $V_b \gg \Delta/e$, where $G \ll G_0$ and $G \approx R_T^{-1}$, respectively, we estimate $G_0 \approx 22\,\mu$S. For each curve in Fig. 1(c) we note the corresponding differential resistance G^{-1}, emphasizing the high sensitivity of the readout at impedances of the order of $1/G_0 \approx 50\,$kΩ. At that impedance the bandwidth, defined as the FWHM of the resonance curve, is 10 MHz and the loaded Q factor is 62.5. In the following we will probe the resonator at resonance.

With the calibrated resonator parameters κ and G_0, a measurement of the transmitted power provides the same information as the conventional current-voltage characteristics of an NIS junction. In particular, such a measurement makes it possible to infer the electronic temperature T_e in the Cu island. To extract T_e from $|s_{21}|^2$, we first convert $|s_{21}|^2$ into G using (1) and then compare the result to the expression for the conductance of the NIS junction

$$G = \frac{1}{R_T k_B T_e} \int dE N_S(E) f(E - eV_b) \left[1 - f(E - eV_b)\right] \ , \qquad (2)$$

where k_B is the Boltzmann constant, e the electron charge, $N_S(E) = \left|\Re{\rm e}\left(E/\sqrt{E^2 - \Delta^2}\right)\right|$ the normalized Bardeen-Cooper-Schrieffer superconducting density of states, $f(E) = [1 + \exp(E/k_B T_e)]^{-1}$ the Fermi function, and Δ is the superconducting gap. Notice that the temperature of the superconducting electrode does not appear in (2); this is a well-known property of the NIS thermometer [22]. Moreover, at the low bias voltages of the thermometer, the backflow of heat from the superconductor is not significant at these temperatures [23].

In Fig. 1(d) we plot $|s_{21}|^2$ as a function of V_b for a set of bath temperatures $T_{\rm bath}$ in the range of 20 to 325 mK. The corresponding T_e versus V_b, as extracted from the traces in the main panel, is plotted in Fig. 1(d), Inset (triangles). We have excluded points around $V_b = \Delta/e$ where the first-order temperature sensitivity vanishes. At base temperature $T_{\rm bath} = 20\,$mK we find that $T_e \approx 85\,$mK. This saturated T_e corresponds to a spurious injected power $\dot{Q}_0 \approx 400\,$aW [21], which we ascribe to imperfect shielding of blackbody radiation as well as low-frequency noise in the dc lines and in the ground potential. The dependence of T_e on V_b, most pronounced for

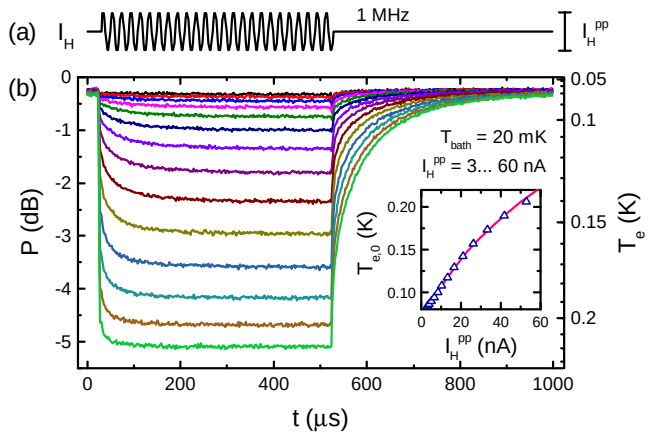

FIG. 2. **Time-resolved thermometry.** (a) Amplitude-modulated sinusoid used to drive the heating pulse (the frequency is not to scale) and (b) real-time response of the thermometer, obtained by recording the transmitted power P versus time for different values of the heating-pulse amplitude $I_H^{\rm pp}$. The conversion from P into absolute electronic temperature T_e is displayed on the right axis. Inset: T_e at the end of the heating pulse ($t = 520\,\mu$s) versus $I_H^{\rm pp}$ (triangles). The prediction of the thermal model [21] is shown for comparison (solid line). All the traces are taken at base temperature by averaging over 10^4 heating cycles and the voltage bias is $V_b = 0.17\,$mV.

the lowest-temperature traces, is due to heat transport across the NIS junction. In particular, cooling is expected to take place when $V_b \approx \Delta/e$ [24], and heating when $V_b \geq \Delta/e$. Conversely, at high temperatures, T_e closely follows $T_{\rm bath}$, as the electron-phonon heat conductance provides a strong thermal anchoring to the electrons in the Cu island. The agreement between T_e and $T_{\rm bath}$ establishes the validity of the rf-NIS electron thermometry. Furthermore, our data are quantitatively accounted for by a simple thermal model which takes the most relevant heat flows into account [21]. The calculated T_e (solid lines) agrees well with the measured ones, except in the vicinity of the optimal cooling point, where only a modest cooling is observed if compared to the theoretical prediction. This behavior can be ascribed to local overheating of the superconductor [25], not included in the model.

TIME-RESOLVED MEASUREMENTS

We demonstrate the real-time capability of our thermometer by measuring the thermal relaxation of the electron gas in the Cu island in response to a Joule heating pulse. The heating pulse is generated by feeding an amplitude-modulated sinusoid of frequency $f_H = 1\,$MHz to a large bias resistor, resulting in an ac heating current of peak-to-peak amplitude $I_H^{\rm pp}$. As f_H is much faster than the measured thermal relaxation rates (see the following), the island reacts to a time-averaged heating power $\dot{Q}_H \propto (I_H^{\rm pp})^2$ when the heating is on. The time-domain response of the thermometer to the heating pulse is shown in Fig. 2(b) at base temperature, for a fixed V_b and different values of $I_H^{\rm pp}$. The left axis indicates the instantaneous power recorded by the digitizer. This power is converted into temperature using a similar procedure as in Fig. 1(d), Inset, and the corresponding scale is noted on the right axis. The temperature reached by the island at the end of the heating pulse is plotted in Fig. 2(b), Inset as a function of $I_H^{\rm pp}$ (triangles), in good agreement with the prediction of the thermal model (solid line). From Fig. 2, we see that the thermal response of the island is not instantaneous; instead, a finite-time relaxation is observed after the rising and falling edge of the pulse.

With constant heat input and when T_e is not far from its steady-state value $T_{e,0}$, the heat equation governing the temperature deviation $\delta T = T_e - T_{e,0}$ can be written as

$$\mathcal{C}\frac{d\delta T}{dt} = -G_{\rm th}\delta T, \qquad (3)$$

where $\mathcal{C}$ is the electronic heat capacity of the island and $G_{\rm th}$ the thermal conductance to its heat bath. Equation (3) tells that T_e relaxes to $T_{e,0}$ exponentially with the relaxation time $\tau = \mathcal{C}/G_{\rm th}$, where $\mathcal{C}$ and $G_{\rm th}$ are to be evaluated at $T_e = T_{e,0}$. Even after a large change in the heating power [beyond the linear-response regime described by (3)], the final approach to the new $T_{e,0}$ obeys this exponential law. The value of $\mathcal{C}$ is ideally given by the standard expression for a Fermi electron gas, $\mathcal{C} = \gamma\mathcal{V}T_{e,0}$, where $\gamma = 71$ JK^{-2}m^{-3} [26] and $\mathcal{V}$ is the volume of the island (in our case, $\mathcal{V} = 0.05\,\mu$m^3). On the other hand, $G_{\rm th}$ is determined by the sum of all relevant parallel heat conductances. In the present case we expect the electron-phonon heat conductance $G_{\rm th,ep}$ and the tunneling heat conductance through the biased NIS junction $G_{\rm th,NIS}$ to be the dominant contributions. Thermal conductivity through the clean NS contacts can be neglected [27] and photonic heat conductance is also negligible for our sample at these temperatures, due to the mismatch of the relevant impedances [28]. Measurements of the heat conductance out of a metallic island were recently reported in [29]. The standard expression for $G_{\rm th,ep}$ is quoted as $G_{\rm th,ep} = 5\Sigma\mathcal{V}T_e^4$ [30]; however, other power laws in T_e have also been reported for experiments on Cu islands [31, 32]. The tunneling heat conductance is given by $G_{\rm th,NIS} = -\frac{1}{e^2R_Tk_BT^2}\int_{-\infty}^{\infty} dE N_S(E)(E-eV)^2 f(E-eV)[1-f(E-eV)]$. For our relatively large island and according to these expressions, we expect $G_{\rm th,ep} \gg G_{\rm th,NIS}$ when the junction is biased far from the gap and $G_{\rm th,ep} \approx G_{\rm th,NIS}$ when V_b approaches Δ/e. However, as indicated by the data in Fig. 1(d), Inset, the cooling performance of the NIS junction is degraded when $V_b \approx \Delta/e$, possibly implying a weaker $G_{\rm th,NIS}$ than pre-

dicted by the model. Finally, it should be mentioned that the electron-phonon relaxation times reported in [12, 31] were longer than those expected based on the expressions above. In addition to a non-ideal $G_{\rm th,ep}$, this may suggest a one order of magnitude larger heat capacity than described by the Fermi gas model, possibly due to magnetic impurities in the metal film [33, 34]. Furthermore, overheating of the local phonon bath, considered in a recent experiment [35], may also lead to longer relaxation times, due to the additional series thermal resistance between the local phonon bath and the thermalized substrate phonons.

We estimate the thermal relaxation times $\tau_{\rm rise}$ and $\tau_{\rm fall}$ by fitting an exponential function to the tails of the relaxation traces observed in Fig. 2 after the rising ($\tau_{\rm rise}$) and falling edge ($\tau_{\rm fall}$) of the heating pulse. More details on the fitting procedure are given in [21]. As we increase the pulse amplitude $I_H^{\rm pp}$, we observe a decrease in $\tau_{\rm rise}$, which is consistent with thermal relaxation to a higher temperature. On the other hand, $\tau_{\rm fall}$ does not depend on $I_H^{\rm pp}$, as expected due to the fact that the relaxation temperature stays the same. We have repeated the measurements of Fig. 2 while varying the bias voltage V_b and the bath temperature $T_{\rm bath}$. The corresponding relaxation times τ are shown in Fig. 3. In panel (a) we show the dependence on V_b for two different values of $T_{\rm bath}$. The measured τ at base temperature is of the order of 100 µs and it increases by some 20% as V_b approaches Δ/e. This increase may well be due to a decrease in $G_{\rm th,ep}$ upon cooling of the island [compare Fig. 1(d), Inset]. In panel (b) we show the temperature dependence of τ, obtained in two independent ways. We first measured $\tau_{\rm fall}$ while varying $T_{\rm bath}$ (circles) and then $\tau_{\rm rise}$ while varying $I_H^{\rm pp}$ (triangles). $\tau_{\rm fall}$ is plotted against $T_{\rm bath}$ and $\tau_{\rm rise}$ is plotted against $T_{e,0}$ at the end of the pulse, estimated as in Fig. 2(b). The agreement between the two series is remarkable. The saturation of τ at low $T_{\rm bath}$ is also consistent with the saturated T_e observed in Fig. 1(d), Inset. From the measured τ we estimate a heat capacity $\mathcal{C} = 2 \cdot 10^5 k_{\rm B} = 3\,{\rm aJ/K}$, one order of magnitude larger than the expected value for a Cu island of the size and temperature in this experiment. At higher temperatures τ is predicted to scale as $T_{e,0}^{-3}$ provided $G_{\rm th} \approx G_{\rm th,ep}$ and both $\mathcal{C}$ and $G_{\rm th,ep}$ follow the theory predictions. The data presented here are not conclusive in this respect, due to the saturation of $T_{e,0}$ at low $T_{\rm bath}$ and to the narrow temperature range considered. This range is not limited by the bandwidth of our thermometer, but rather by a transient that we observe after terminating the heat pulse, possibly due to the heavy low-pass filtering applied to the heating line. For this reason, we refrain from presenting data points with $\tau \lesssim 20\,\mu$s and leave the study of relaxation times down to 1 µs and below to future investigation.

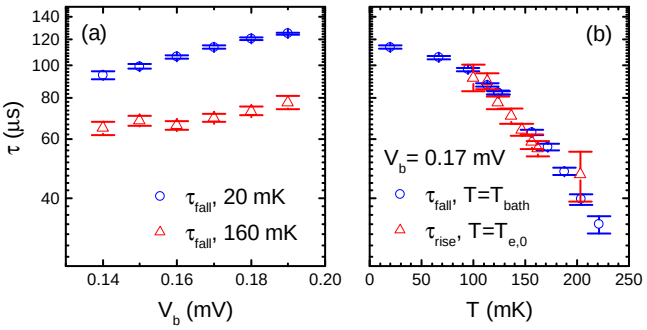

FIG. 3. **Thermal relaxation times.** (a) Thermal relaxation time τ versus voltage bias V_b for two different values of the bath temperature $T_{\rm bath}$. (b) Temperature dependence of τ, as estimated from relaxation after the falling edge (circles, the x axis is $T_{\rm bath}$) as well as the rising edge of the pulse (triangles, the x axis is the temperature $T_{e,0}$ at the end of the pulse). The error bars are obtained from the fits (see [21]).

NOISE AND RESPONSIVITY

We have performed an extensive characterization of the responsivity and noise of the thermometer readout. Our first set of experiments, presented above, were performed at low input powers corresponding to a voltage modulation amplitude across the NIS junction of the order of 1 µV. In this case, the readout probes the local differential conductance of the junction. Accordingly, the theoretical responsivity $\mathcal{R} = \partial P_{\rm det}/\partial T_e$ of the thermometer is $\mathcal{R} \propto P_{\rm gen}(\partial|s_{21}|^2/\partial G)(\partial G/\partial T_e)$. We evaluate the noise-equivalent temperature (NET) as $(\delta P_{\rm det}/\delta T)^{-1}(\sqrt{S_{P_{\rm det}P_{\rm det}}})$, where $S_{\rm P_{det}P_{det}}$ is the measured noise spectral density of the detected power $P_{\rm det}$. At an electron temperature of 80 mK and at the optimal bias point of 0.17 mV, we obtain our best NET of $90\,\mu{\rm K}/\sqrt{\rm Hz}$. We always find an essentially white noise spectrum, with a corner frequency for $1/f$ noise of the order of a few Hz.

The thermometer readout was amplifier-limited. We characterize the noise of the rf readout chain by the system noise temperature $T_{\rm sys}$ referred to the output port of the sample box. In this case (see supplement for details [21]), one has $S_{P_{\rm det}P_{\rm det}} \approx 4Gk_BT_{\rm sys}P_{\rm det}$, where $G = P_{\rm det}/P_{\rm out}$ is the total gain of the amplification chain. Using power-dependent features of the NIS-junction-loaded resonator as markers, we estimate $G = 55 \pm 1$ dB and $T_{\rm sys} = 62 \pm 15$ K. The discrepancy between $T_{\rm sys}$ and the nominal noise temperature of the HEMT amplifier, 13.3 K at 640 MHz, suggests an insertion loss of the order of 7 dB between the resonator and the amplifier.

Assuming the heat conductance $G_{\rm th}$ to be dominated by electron-phonon interaction [as indicated by the steady-state measurements of Fig. 1(d)], the noise-equivalent power (NEP) is given by ${\rm NEP} = {\rm NET}\,G_{\rm th} =$

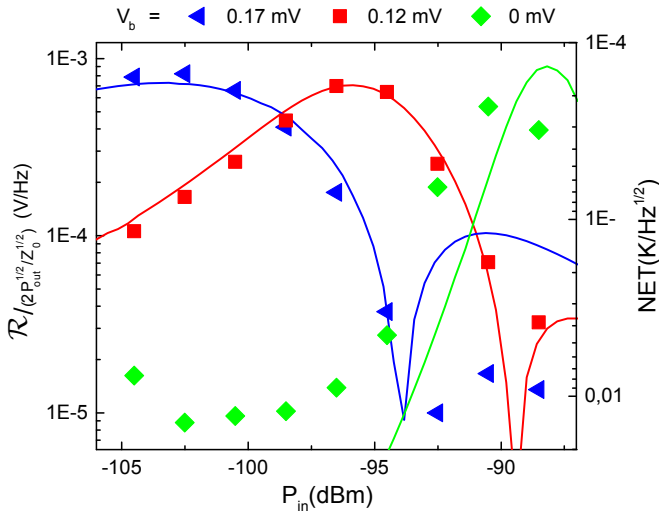

FIG. 4. **Power optimization.** Normalized responsivity $\mathcal{R}$ (left axis) and corresponding noise-equivalent temperature (right axis) versus $P_{\rm in}$ for three selected bias voltages (symbols), measured at 150 mK. Numerical simulations are shown for comparison (solid lines, see [21] for details).

$2.5 \times 10^{-18}\,\mathrm{W}/\sqrt{\mathrm{Hz}}$. This figure is one order of magnitude above the thermal fluctuation noise limit $\mathrm{NEP_{th}} = \sqrt{4k_B T_e^2 G_{\rm th}} = 1 \times 10^{-19}\,\mathrm{W}/\sqrt{\mathrm{Hz}}$.

One may ask whether the NET figure given above can be significantly improved by operating the rf-NIS thermometer at higher input powers, *i.e.*, beyond the linear regime. In Fig. 4 we compare the responsivity and NET of our thermometer at different bias voltages and as a function of the power fed to the input line. The data (symbols) were taken in a separate cooldown using an equivalent setup and a sample with $R_T = 28\,\mathrm{k}\Omega$. The optimal power increases as the bias point is shifted towards zero bias. Importantly, a sensitivity close to the global optimum ($144\,\mu\mathrm{K}/\sqrt{\mathrm{Hz}}$ for this sample at $T_{\rm bath} = 150$ mK) is reached over a broad range of bias voltages by a suitable choice of probing power. This feature can be understood by considering the combined contribution of the dc bias and the rf drive to the instantaneous voltage across the junction, and the fact that the responsivity of the NIS thermometer is concentrated in a narrow voltage range slightly below the superconducting gap edge. Indeed, full numerical simulations (solid lines) confirm this behavior.

OUTLOOK

In summary, we have demonstrated an electronic thermometer with promise for ultralow-energy calorimetry, operating below 100 mK, with $90\,\mu\mathrm{K}/\sqrt{\mathrm{Hz}}$ noise-equivalent temperature and 10 MHz bandwidth. We have measured thermal relaxation times up to 100 µs, in line with 1.6 – 20 µs measured by other methods at higher temperatures [12, 31]. These figures already enable single-shot detection of an energy-absorption event producing a 10 mK temperature spike. Such a spike could be generated, for instance, by a single THz photon impinging of an absorber of reduced volume, as well as by a multi-photon wave packet in the C and X band used for superconducting-quantum-bit readout [37–39]. In absolute terms, the NEP performance of our device still lags behind that of state-of-the-art transition-edge sensors [40, 41] and semiconductor bolometers [42, 43], which routinely achieve NEPs of the order of $10^{-20}\,\mathrm{W}/\sqrt{\mathrm{Hz}}$. However, most of these devices are intended for detection of THz radiation, while our primary focus is on microwave photons. In the microwave domain, our approach presents some advantages; in particular, our sensor can be straightforwardly integrated in superconducting coplanar waveguides, acting as a lumped-element resistor whose impedance can be made to be of the order of $50\,\Omega$.

Our current device and set-up leave room for improvement. Calculations indicate that the sensitivity of a fully optimized NIS thermometer can reach $\mathrm{NET_{opt}} = \sqrt{2.72 \mathrm{e}^2 T_{\rm sys} R_{\rm T}/k_{\rm B}}$. Using the parameters for our primary sample ($R_{\rm T} = 22\,\mathrm{k}\Omega$) and present set-up ($T_{\rm sys} = 62$ K), this formula yields $\mathrm{NET_{opt}} = 83\,\mu\mathrm{K}/\sqrt{\mathrm{Hz}}$, to be compared with our experimental value of $90\,\mu\mathrm{K}/\sqrt{\mathrm{Hz}}$. We conclude that the impedance matching between the NIS junction and the transmission line realized by the resonator was close to optimal. Instead, the system noise temperature could be lowered by more than an order of magnitude by reducing losses between the sample box and the amplifier and by employing an amplifier with a lower noise temperature as the first stage; a Josephson parametric amplifier [44] is one such choice. The energy resolution of our detector can be estimated as $\delta E = \mathcal{C}\,\delta T = \mathrm{NET}\,\mathcal{C}\,\tau^{-1/2}$. For the present case this gives $\delta E = 2.3 \cdot 10^{-20}$ J, corresponding to a photon of frequency $\delta E/h = 34\,\mathrm{THz}$. The measured sample was not optimized for obtaining a small energy resolution; instead, we aimed at a strong coupling between the island and the phonon bath. In order to boost energy resolution, the size of the island can be made significantly smaller, which is the next step toward improving this device. When the noise is limited by thermal fluctuations, we can write $\delta E = \sqrt{4k_{\rm B}\mathcal{V}\gamma^2/(5\Sigma\tau)}$. For a sample with 50 times smaller island limited by thermal fluctuations, the energy resolution at 80 mK, assuming 100 μs relaxation time, is $\delta E/h = 30\,\mathrm{GHz}$. Since τ increases strongly with decreasing temperature, lowering the island temperature is another key point. Optimized as indicated, our detector will facilitate a series of experiments of fundamental relevance in classical and quantum thermodynamics, as well as calorimetric measurements of dissipation down to single microwave photons in superconducting quantum circuits.

ACKNOWLEDGEMENTS

We would like to thank A. Adamyan, S. Kubatkin, J. Govenius, R. Lake and J. Peltonen for useful discussions and S. Kafanov for technical assistance at an early stage of the project. This work has been supported in part by the Academy of Finland (project no. 139172) and its LTQ (project no. 250280), and the European Union Seventh Framework Programme INFERNOS (FP7/2007-2013) under grant agreement no. 308850. S. G. acknowledges financial support from the Finnish National Graduate School in Nanoscience (NGS-NANO) and from the Aalto Doctoral Programme in Science.

* simone.gasparinetti@aalto.fi

† klaara.viisanen@aalto.fi

[1] K. Schwab, E. A. Henriksen, J. M. Worlock, and M. L. Roukes, Nature **404**, 974 (2000).

[2] M. Meschke, W. Guichard, and J. P. Pekola, Nature **444**, 187 (2006).

[3] S. Jezouin, F. D. Parmentier, A. Anthore, U. Gennser, A. Cavanna, Y. Jin, and F. Pierre, Science **342** 601 (2013).

[4] A. Bérut, A. Arakelyan, A. Petrosyan, S. Ciliberto, R. Dillenschneider, and E. Lutz, Nature **483**, 187 (2012).

[5] S. Toyabe, T. Sagawa, M. Ueda, E. Muneyuki, and M. Sano, Nat. Phys. **6**, 988 (2010).

[6] J. V. Koski, V. F. Maisi, J. P. Pekola, and D. V. Averin, PNAS **111**, 13786 (2014).

[7] J. P. Pekola, P. Solinas, A. Shnirman, and D. V. Averin, New J. Phys. **15**, 115006 (2013).

[8] S. Gasparinetti, P. Solinas, A. Braggio, and M. Sassetti, New J. Phys. **90**, 064505 (2014).

[9] M. Silaev, T. T. Heikkilä, and P. Virtanen, Phys. Rev. E **90**, 022103 (2014).

[10] M. Nahum and J. M. Martinis, Appl. Phys. Lett. **66**, 3203 (1995).

[11] D. R. Schmidt, C. S. Yung, and A. N. Cleland, Appl. Phys. Lett. **83**, 1002 (2003).

[12] D. R. Schmidt, C. S. Yung, and A. N. Cleland, Phys. Rev. B **69**, 140301(R) (2004).

[13] D. R. Schmidt, K. W. Lehnert, A. M. Clark, W. D. Duncan, K. D. Irwin, N. Miller, and J. N. Ullom, Appl. Phys. Lett. **86**, 053505 (2005).

[14] J. M. Rowell and D. C. Tsui, Phys. Rev. B **14**, 2456 (1976).

[15] M. Nahum and J. M. Martinis, Appl. Phys. Lett. **63**, 3075 (1993).

[16] F. Giazotto, T. T. Heikkilä, A. Luukanen, A. M. Savin, and J. P. Pekola, Rev. Mod. Phys. **78**, 217 (2006).

[17] R. J. Schoelkopf, P. Wahlgren, A. A. Kozhevnikov, and D. E. Prober, Science **280**, 1238 (1998).

[18] H. Qin and D. A. Williams, Appl. Phys. Lett. **88**, 203506 (2006).

[19] D. J. Reilly, C. M. Marcus, M. P. Hanson, and A. C. Gossard, Appl. Phys. Lett. **91**, 162101 (2007).

[20] O.-P. Saira, A. Kemppinen, V. F. Maisi, and J. P. Pekola, Phys. Rev. B **85**, 012504 (2012).

[21] See Supplemental Material at [url].

[22] H. Pothier, S. Guéron, N. O. Birge, D. Esteve, and M. H. Devoret, Phys. Rev. Lett. **79**, 3490 (1997).

[23] J. Muhonen, M. Meschke, and J. P. Pekola, Rep. Prog. Phys. **75**, 046501 (2012).

[24] M. Nahum, T. M. Eiles, and J. M. Martinis, Appl. Phys. Lett. **65**, 3123 (1994).

[25] S. Rajauria, H. Courtois, and B. Pannetier, Phys. Rev. B **80**, 214521 (2009).

[26] B.W. Roberts, *Properties of Selected Superconductive Materials*, NBS Technical Note 983, U.S Government Printing Office (1978).

[27] J. T. Peltonen, P. Virtanen, M. Meschke, J. V. Koski, T. T. Heikkilä, and J. P. Pekola, Phys. Rev. Lett. **105**, 097004 (2010).

[28] A. V. Timofeev, M. Helle, M. Meschke, M. Möttönen, and J. P. Pekola, Phys. Rev. Lett. **102**, 200801 (2009).

[29] J. Govenius, R. E. Lake, K. Y. Tan, V. Pietilä, J. K. Julin, I. J. Maasilta, P. Virtanen, and M. Möttönen, preprint available on arXiv:1403.6586 .

[30] F. C. Wellstood, C. Urbina, and J. Clarke, Phys. Rev. B **49**, 5942 (1994).

[31] L. J. Taskinen, J. M. Kivioja, J. T. Karvonen, and I. J. Maasilta, phys. stat. sol. (c) **1**, 2856 (2004).

[32] J. T. Karvonen, L. J. Taskinen, and I. J. Maasilta, Phys. Rev. B **72**, 012302 (2005).

[33] F. Pobell, *Matter and methods at low temperatures*, 3rd ed., Springer (2007).

[34] A. Anthore, F. Pierre, H. Pothier, and D. Esteve, Phys. Rev. Lett. **90**, 076806 (2003).

[35] L. M. A. Pascal, A. Fay, C. B. Winkelmann, and H. Courtois, Phys. Rev. B **88**, 100502 (2013).

[36] A small ($< 2\%$) baseline correction is applied to correct for a slow, much weaker relaxation process of unknown origin. See [21] for details.

[37] A. Wallraff, D. I. Schuster, A. Blais, L. Frunzio, R. S. Huang, J. Majer, S. Kumar, S. M. Girvin, and R. J. Schoelkopf, Nature **431**, 162 (2004).

[38] A. A. Houck, D. I. Schuster, J. M. Gambetta, J. A. Schreier, B. R. Johnson, J. M. Chow, L. Frunzio, J. Majer, M. H. Devoret, S. M. Girvin, and R. J. Schoelkopf, Nature **449**, 328 (2007).

[39] D. Bozyigit, C. Lang, L. Steffen, J. M. Fink, C. Eichler, M. Baur, R. Bianchetti, P. J. Leek, S. Filipp, M. P. da Silva, A. Blais, and A. Wallraff, Nat. Phys. **7**, 154 (2010).

[40] B. S. Karasik and R. Cantor, Appl. Phys. Lett. **98**, 193503 (2011).

[41] B. S. Karasik, A. V. Sergeev, and D. E. Prober, IEEE Trans. Terahertz Sci. Technol. **1**, 97 (2011).

[42] S. Komiyama, O. V. Astafiev, V. Antonov, T. Kutsuwa, and H. Hirai, Nature 403, 405 (2000).

[43] S. Komiyama, IEEE J. Sel. Top. Quantum Electron. 17, 54 (2011).

[44] M. A. Castellanos-Beltran and K. W. Lehnert, Appl. Phys. Lett. **91**, 083509 (2007).

Supplemental Material for "Fast electron thermometry towards ultra-sensitive calorimetric detection"

THERMAL MODEL

In order to estimate the steady-state electronic temperature T_e, we numerically solve a power-balance equation of the conventional form

$$\dot{Q}_{\rm ep}(T_e, T_{\rm bath}) + \dot{Q}_{\rm NIS}(V_b, T_e) + \dot{Q}_H(V_H) + \dot{Q}_0 = 0 \ . \tag{4}$$

Here, we take temperature relaxation via electron-phonon coupling to be given by the standard expression $\dot{Q}_{\rm ep} = \Sigma\mathcal{V}(T_e^5 - T_{\rm bath}^5)$, where $\Sigma = 2\times10^9\,{\rm Wm^{-3}K^{-5}}$ is the electron-phonon interaction constant, $\mathcal{V}$ is the island volume and we assume the local phonons to be termalized at the bath temperature $T_{\rm bath}$. The heat flow into the island due to electron tunneling through the NIS junction is given by

$$\dot{Q}_{\rm NIS} = -\frac{1}{e^2R_T}\int_\Delta^\infty dE N_S(E)\left[(E-eV_b)f_N(E-eV_b) + (E+eV_b)f_N(E+eV_b) - 2Ef_S(E)\right] \ , \tag{5}$$

where V_b is the voltage bias, $R_T = 22\,{\rm k\Omega}$ is the tunneling resistance of the junction, f is the Fermi function, the subscripts N and S refer to the normal and superconducting electrode, respectively, and N_S is the BCS density of states. The last two terms in (5) can be neglected provided $k_BT_{N,S} < 0.3\Delta$, where Δ is the zero-temperature superconducting gap. The power fed through the heating line is $\dot{Q}_H(V_H) = V_H^2 r_I/R_H^2$, where V_H is the heating voltage, $R_H = 3\,{\rm M\Omega}$ is the room-temperature bias resistor and $r_I = 360\,\Omega$ the total resistance of the island. Finally, we assume that some spurious, constant heating power $\dot{Q}_0$ is delivered to the island due to imperfect filtering. There are two free parameters in the model: Δ and $\dot{Q}_0$. In particular, the value $\Delta = 213\,{\rm \mu eV}$, in good agreement with other measurements on thin Al films, can be inferred from the crossing point of the curves in Fig. 1(d) in the main text. The value $\dot{Q}_0 = 400\,{\rm aW}$ essentially determines the value of T_e observed at low $T_{\rm bath}$. All the theoretical curves in Fig. 1(d), Inset in the main text were produced using these values for Δ and $\dot{Q}_0$.

ANALYSIS OF THERMAL RELAXATION TIMES

In Fig. 5, we present relaxation tails obtained from measurements similar to those presented in Fig. 2 in the main text. The tails are obtained from the raw data by subtracting the steady-state-temperature baseline from each trace. They have been normalized, horizontally offset for clarity, and plotted in a semilogarithmic scale in order to highlight the exponential decay. The full lines are fits of an exponential function to the tails. The tails in panels (a,b) refer to relaxation after the rising (a) and falling edge (b) of heating pulses of different amplitude $I_H^{\rm pp}$. As $I_H^{\rm pp}$ is increased, relaxation after the rising edge gets faster as $T_{e,0}$ increases; on the other hand, no change is observed in the tails after the falling edge, as $T_{e,0}$ stays the same. In panel (c), we vary the bath temperature $T_{\rm bath}$ and see that the relaxation gets faster as $T_{\rm bath}$ is increased. In panel (d), we vary the bias voltage V_b. The observed time constant stays approximately the same, regardless of the fact that G changes by over two orders of magnitude across the given V_b range.

LONG TIME SCALE IN THE RELAXATION TRACES

Besides the relaxation mechanism discussed in the previous section, our data show evidence of another, much weaker relaxation process taking place on a longer time scale. In Fig. 6 we show an extended time trace after the heating pulse, averaged over one million repetitions (dots). The full line is obtained by fitting a double exponential of the form $A_1\exp(-t/\tau_1) + A_2\exp(-t/\tau_2)$ to the data. The fitted relaxation times are $\tau_1 = 97\,{\rm \mu s}$ (the main relaxation) and $\tau_2 = 0.41\,{\rm ms}$; the ratio between the two amplitudes is $A_2/A_1 = 0.018$. The origin of the slower relaxation process is presently unknown to us; however, the separation between the two time scales allows us to ignore the time dependence of the slower process during the thermal relaxation over τ_1. For this reason, in the main text we fit a single exponential to the data with a corrected baseline. The baseline correction does not exceed 2% in the data presented.

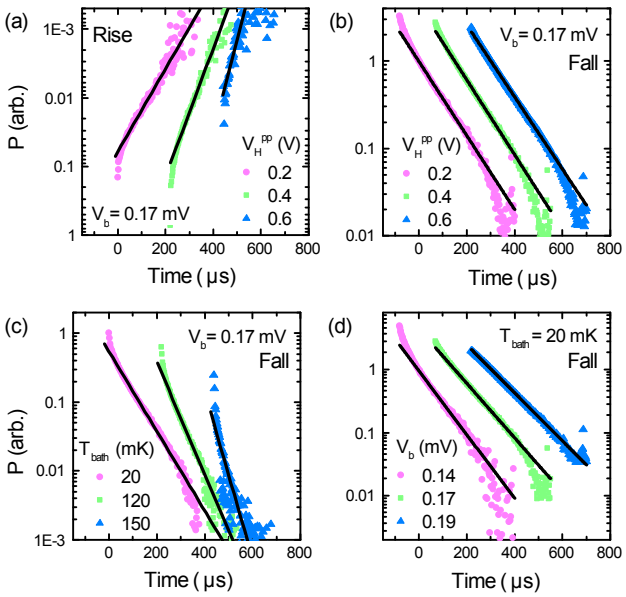

FIG. 5. Thermal relaxation traces (circles, squares, triangles). The traces are shifted by their baseline after relaxation, scaled and plotted on a logarithmic scale. They are also horizontally offset by 150 μs for clarity. The full lines are exponential fits of the form $A\exp(t/\tau)+B$ to the data. The data in panels (a,b) correspond to the rising (a) and falling edges (b) of selected traces in Fig. 2 of the main text. Panels (c,d) present similar traces obtained at different bath temperatures $T_{\rm bath}$ (c) and for different values of the voltage bias V_b (d). All the traces are obtained by averaging over $2\cdot 10^5$ heating cycles.

POWER OPTIMIZATION

In order to measure the temperature sensitivity of our thermometer beyond linear-response, we proceed in the following manner. We first apply a continuous heating signal of varying amplitude $I_H^{\rm pp}$ to the island and measure temperature by using the thermometer in the liner response. Using the calibration of the resonator and the model for the NIS junction, we calibrate the island temperature against $I_H^{\rm pp}$. We then repeat the measurement for various input powers. Using the $I_H^{\rm pp}$-to-temperature calibration, we extract the temperature responsivity as $\partial P_{\rm det}/\partial T = (\partial P_{\rm det}/\partial I_H^{\rm pp})(\partial I_H^{\rm pp}/\partial T)$, where $P_{\rm det}$ is the measured mean power. After measuring the noise spectral density $S_{P_{\rm det}P_{\rm det}}$,

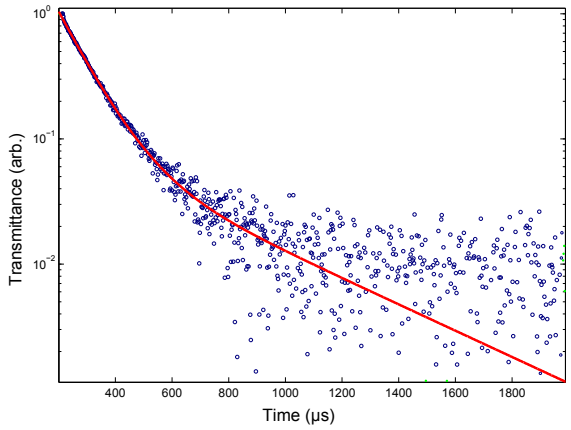

FIG. 6. Detail of a 10 ms long time trace taken under the same conditions as in Fig. 3 of the main text (dots). The full line is a fit of a double exponential $A_1\exp(-t/\tau_1)+A_2\exp(-t/\tau_2)$ to the data.

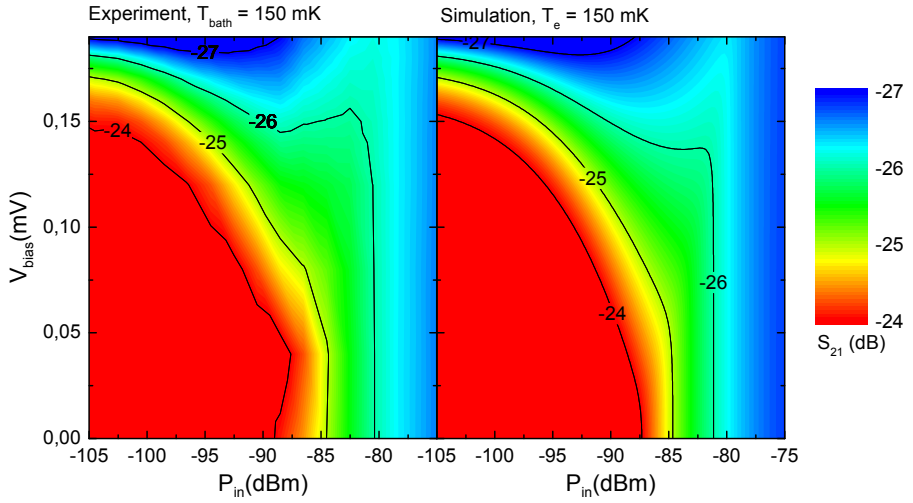

FIG. 7. Measured (left) and simulated (right) transmittance of power $|S_{21}|^2 = P_{\rm det}/P_{\rm gen}$ as a function of $P_{\rm in}$ and $V_{\rm b}$.

we finally estimate the sensitivity as $\sqrt{S_{P_{\rm det}P_{\rm det}}}(\partial P_{\rm det}/\partial T)^{-1}$.

In Fig. 4 in the main text, we compare the estimated sensitivity to numerical simulations. The simulations fully take into account the nonlinear current-voltage characteristics of the NIS junction and use the harmonic balance method to determine the response of the resonator terminated with the junction to a harmonic excitation of arbitrary amplitude. The power incident at the sample box $P_{\rm in}$ is obtained by subtracting the total attenuation (A) of the input chain from the output power of the signal generator $P_{\rm gen}$. Comparing the simulated $|s_{21}|^2$ with measurements as a function of $P_{\rm in}$ and $V_{\rm b}$ (see Fig. 7) allows us to estimate $A = 77.5 \pm 1$ dB, and the gain of the output chain, $G = 55 \pm 1$ dB.

NOISE MEASUREMENT

We acquire real-time traces by demodulating the signal at the carrier frequency f_0 and recording the output with a fast digitizer. As a result, we obtain a power-versus-time trace over a bandwidth B which is proportional to the sampling rate f_S. If we assume the readout to be limited by the noise of our amplification chain, rather than by the intrinsic noise of our device, due to, e. g., effective temperature fluctuations – this assumption is verified *a posteriori* –, we can express $P_{\rm det}$ and $S_{P_{\rm det}P_{\rm det}}$ as:

$$\begin{aligned} P_{\rm det} &= P_s + BGS_a \ , \\ S_{P_{\rm det}P_{\rm det}} &= -2BG^2S_a^2 + 4GS_aP_{\rm det} \ , \end{aligned} \tag{6}$$

where P_s is the signal without the noise and S_a is the spectral density of the amplifier noise. From (6) we see that $P_{\rm det}$ is offset by a constant amount, proportional to the bandwidth times the amplifier noise. Furthermore, the noise S_{PP} has a contribution which is proportional to $P_{\rm det}$.

In Fig. 8 we investigate the linear relationship between $S_{P_{\rm det}P_{\rm det}}$ and $P_{\rm det}$ by measurements taken at different voltage biases and input powers. From a linear fit we extract $4GS_a = 1.2 \times 10^{-15}$ W/Hz, so that $GS_a = 3.0 \times 10^{-16}$ W/Hz. The noise temperature of the chain is $T_{\rm sys} = 62 \pm 15$ K.

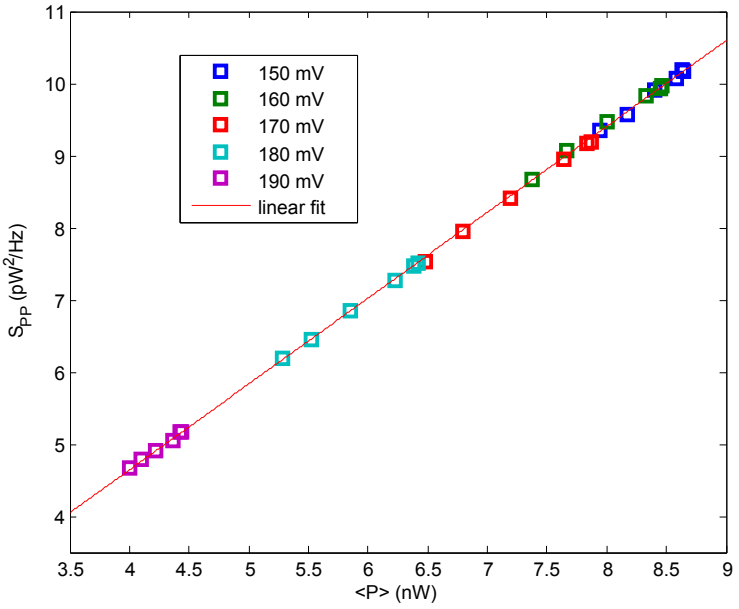

FIG. 8. Power noise spectral density $S_{P_{\rm det}P_{\rm det}}$ versus mean power $P_{\rm det}$. The data are taken at $T_e = 126$ mK for different bias voltages $V_{\rm b}$ (see the legend) and different input powers. The sampling rate is $f_s = 0.5\,\mathrm{MS/s}$.